

A dendrite-resolved, *in vivo* transfer function from spike patterns to dendritic Ca^{2+}

Xiang Wu¹, Byung Hun Lee¹, Pojeong Park^{1,2}, J. David Wong-Campos^{1,3}, Junjie Xu¹, Sarah E. Plutkis³, Luke D. Lavis³, Adam E. Cohen^{1,4}

¹ Department of Chemistry and Chemical Biology, Harvard University, Cambridge, MA, USA

² Department of Brain Sciences, DGIST, Daegu, Republic of Korea

³ Janelia Research Campus, Howard Hughes Medical Institute, Ashburn, Virginia, USA

⁴ Department of Physics, Harvard University, Cambridge, MA, USA

Contact: cohen@chemistry.harvard.edu

Abstract

Dendrites transform local electrical activity into intracellular Ca^{2+} signals that drive plasticity^{1,2}, yet the voltage $\rightarrow\text{Ca}^{2+}$ mapping during natural behavior remains poorly defined. Here, we measure this transfer function via simultaneous voltage and Ca^{2+} imaging throughout the dendritic arbors of hippocampal CA2 pyramidal neurons in behaving mice. Dendritic Ca^{2+} exhibited a hierarchical activation pattern dominated by back-propagating action potentials: simple spikes primarily drove somatic and proximal Ca^{2+} , whereas complex spikes produced larger somatic Ca^{2+} signals and propagated farther into distal dendrites, sometimes in a branch-selective manner. Dendrite-restricted co-activation of voltage and Ca^{2+} without concurrent somatic events was rare. A biophysics-inspired model accurately predicted local Ca^{2+} transients from local voltage waveforms. Our data and model provide a quantitative understanding of when – and why – dendritic Ca^{2+} signals in CA2 pyramidal cells arise during behavior.

Introduction

The conversion of electrical activity into changes in intracellular Ca^{2+} concentration is the key electrical-chemical coupling step in the nervous system. In dendrites, several types of electrical excitations activate local Ca^{2+} influx^{3–7}. This Ca^{2+} is the principal node linking dendritic activation to synaptic plasticity^{1,2}, retrograde signaling⁸, and in some cases excitotoxicity⁹.

In vivo, dendritic Ca^{2+} imaging has therefore become a widely used approach for probing dendritic activity^{10–13}. Yet Ca^{2+} is an imperfect proxy for electrical excitation. Ca^{2+} transients are \sim 100-fold slower than the underlying voltage events that evoke them, and the mapping from voltage to Ca^{2+} is nonlinear and history-dependent. As a result, similar Ca^{2+} waveforms can arise from distinct electrical patterns (or with no concurrent electrical event at all¹⁴), and functionally important subthreshold electrical events may not evoke detectable Ca^{2+} . These features complicate efforts to infer parameters of dendritic computation or physiology from Ca^{2+} imaging alone.

The dendritic voltage-to- Ca^{2+} transfer function is subject to several layers of dynamic regulation: Ca^{2+} enters through voltage-gated Ca^{2+} channels¹⁵ and NMDA receptors¹⁶, while Ca^{2+} -activated K^+ channels¹⁷ and slower Ca^{2+} -dependent signaling pathways¹⁸ feed back onto voltage and excitability. Intracellular Ca^{2+} is further sculpted by strong buffering, uptake by mitochondria¹⁹, and amplification through Ca^{2+} -induced Ca^{2+} release from the endoplasmic reticulum²⁰. Together, these coupled mechanisms raise the possibility that dendritic Ca^{2+} reports a mixture of

backpropagating action potentials, locally generated spikes, synaptic inputs, and compartmental biochemical amplification.

Slice physiology established early constraints on the voltage-to- Ca^{2+} mapping. In acute brain slices, the extent to which somatic Na^+ spikes backpropagate into CA1 pyramidal apical dendrites governs how far Ca^{2+} elevations propagate, and this coupling depends on firing history^{15,21–23}. Other slice experiments showed that clustered synaptic input can evoke Ca^{2+} excitations confined to apical dendrites²⁴, and that dendritically generated events such as NMDA spikes and plateau potentials can produce large, long-lasting depolarizations accompanied by substantial apical Ca^{2+} entry^{15,22,24} and burst firing²⁵. *In vivo*, NMDA-dependent plateau potentials are associated with burst firing^{26–28}, place-field structure, and plasticity^{29–31}. However, the spatiotemporal patterns of electrical events that give rise to these Ca^{2+} dynamics remain poorly defined during natural behavior.

Given the different dynamical regimes of neural activity in slices vs. *in vivo*, one may not confidently extrapolate the voltage– Ca^{2+} mapping from reduced preparations. Despite the centrality of this mapping for interpreting dendritic Ca^{2+} signaling, only a few studies have directly measured dendritic voltage and Ca^{2+} simultaneously *in vivo*^{32,33}, and these studies only probed a small portion of the dendritic arbor. Establishing the voltage-to- Ca^{2+} transfer function across the full dendritic arbor under naturalistic conditions is therefore essential for interpreting dendritic Ca^{2+} signals and for understanding how dendritic electrical events are converted into the biochemical signals that drive plasticity.

Hippocampal area CA2 is a specialized brain region which appears to be a hub for social memory³⁴. Though the electrophysiology of pyramidal cells in this brain region is not as thoroughly studied as in neighboring CA1 and CA3, dendrites of CA2 pyramidal cells are known to be excitable^{35,36}, and apical excitations are implicated in plasticity of inputs from entorhinal cortex³⁷. The apical dendrites of CA2 pyramidal cells branch close to the soma, increasing the possibility of branch-specific electrical signaling and Ca^{2+} dynamics. Thus CA2 is a good model for studying the voltage-to- Ca^{2+} transfer function with direct relevance to dendrite-specific plasticity rules.

Results

Simultaneous voltage and Ca^{2+} imaging in dendrites of behaving mice

We developed a hybrid structured illumination spinning disk confocal microscope which provided kilohertz frame-rate optically sectioned imaging in two colors, with enhanced background rejection compared to structured illumination or spinning disk alone (**Fig. 1a**, **Fig. S1**). Separate digital micromirror devices (DMDs) patterned the red (607 nm, for voltage imaging) and blue (488 nm, for Ca^{2+} imaging) excitation lasers. These beams were then combined and re-imaged onto the microlens array of the spinning disk (**Methods**). The DMD patterns were designed to restrict illumination to the dendrites of interest, and to block illumination of interstitial regions.

The spinning disk confocal and the DMD-patterned illumination worked synergistically: the spinning disk pinholes rejected light from outside the focal plane; the DMD patterning reduced diffuse background from multiply-scattered photons. Together, these two approaches achieved significantly higher contrast and signal-to-noise ratio compared to patterned illumination or spinning disk alone (**Fig. S1h,i**). Similar contrast enhancement has been demonstrated with other hybrid confocal/targeted illumination systems³⁸.

In the image path, a dichroic beamsplitter directed the Ca^{2+} signal to one camera and the voltage signal to a second camera. To achieve imaging at 1 kHz, we implemented phase-locked hardware synchronization between the voltage-imaging camera frame-clock and the spinning disk rotation³⁹. We also implemented post-acquisition computational correction for slight variations between the twelve spinning disk sectors (**Fig. S2, Methods**). The Luminos software provided sub-pixel mapping of DMD to camera coordinates and microsecond-precision coordination of the whole experiment⁴⁰. The image processing pipeline is described in **Methods** and **Fig. S3**.

We co-expressed the red chemogenetic voltage indicator Voltron2-JF608 and the green Ca^{2+} indicator jGCaMP8m in hippocampal pyramidal cells of adult mice (**Fig. 1b, Methods**)^{41,42}. A Lucy-Rho sequence was added to Voltron2 to improve its trafficking in dendrites^{43,44}. We implanted a custom microprism to provide optical access to a sagittal transect of the hippocampus (**Fig. 1c, Methods**)⁴⁵. While the prism field of view spanned CA1 and CA2, we found that the reporter constructs expressed better in the CA2 neurons, so we focused on these. Dendritic trees of individual early-bifurcating CA2 pyramidal cells (**Fig. S4**)^{35,46} were clearly resolved from soma to apical tuft (**Fig. 1d**).

We verified via immunostaining for reactive astrocytes that the tissue damage was confined to $\sim 30 \mu\text{m}$ adjacent to the prism face (**Fig. S5**), consistent with prior microprism studies demonstrating stable chronic optical access and preserved tissue health beyond the interface zone^{47,48}. We imaged neurons at distances of 50 – 150 μm from the prism face, where reactivity was minimal. The prism implantation location and orientation were selected to minimize interference with axonal connections to the recorded neurons⁴⁹. Recent work showed that this prism preparation does not alter neuronal firing or place-field properties relative to the dorsal cannula preparation commonly used for *in vivo* hippocampus imaging⁴⁹.

We combined the optical and molecular tools to map the spontaneous voltage (1 kHz) and Ca^{2+} (41.5 Hz) dynamics across the dendritic trees of pyramidal neurons while mice walked along a linear track in a 2-m virtual reality (VR) visual environment. These recordings clearly resolved subthreshold voltage dynamics, simple spikes, and complex spikes throughout the dendritic tree, as well as the accompanying Ca^{2+} events (**Fig. 1e,f, Supplementary Video 1**). Recordings typically lasted 10 minutes. During this time, photobleaching caused the Voltron2 fluorescence to decay to $71 \pm 5\%$ of its initial amplitude (mean \pm s.d., $n = 12$ cells), and the jGCaMP8m fluorescence to decrease to $75 \pm 6\%$ of its initial amplitude. These decays were corrected in post-processing. Though Ca^{2+} events were detected based on the jGCaMP8 signal alone, all detected Ca^{2+} events ($n = 1282$ events over 12 cells, 9 mice) had a corresponding electrical excitation, confirming that false-positive detections were unlikely. In the apical tuft, where jGCaMP8m fluorescence was dimmest, complex spike-evoked Ca^{2+} events had a signal-to-noise ratio (SNR) of 17.7 ± 4.6 (mean \pm s.d.), 5.9-fold larger than the event-detection threshold set at SNR = 3 (**Methods**).

Ca^{2+} in apical dendrites primarily comes from complex spikes

We first explored the Ca^{2+} footprints of different types of voltage events. Single action potentials (simple spikes, SSs) reliably induced Ca^{2+} transients at the soma and proximal dendrites (**Fig. 2a-c**). The peak voltage from an SS (measured as $\Delta F/F$) decayed with distance along the apical

dendrites with a length constant $306 \pm 50 \mu\text{m}$ (mean \pm s.d., $n = 493$ events, 10 neurons, 7 mice, **Fig. S6**). The peak Ca^{2+} signal of the same events decayed with a length constant $187 \pm 46 \mu\text{m}$ (**Fig. S6**). While the voltage signal from an SS was clearly detectable in the most distal dendrites (483 μm from the soma), there was no detectable Ca^{2+} signal in these dendrites.

We then explored events with more spikes. We defined successive spikes as belonging to the same event if all inter-spike intervals were $\leq 25 \text{ ms}$. Events with 4 or more spikes riding atop a subthreshold depolarization at the soma were classified as complex spikes (CSs, **Fig. 2c, Methods**). The somatic Ca^{2+} signal was an increasing, but sub-linear, function of the number of spikes in an event (**Fig. 2a,b**), consistent with recent simultaneous patch-clamp and jGCaMP8m recordings *in vivo*⁴². Events with ≤ 3 spikes did not induce detectable Ca^{2+} signal in the distal apical dendrites ($> 350 \mu\text{m}$ from the soma, **Fig. 2a,b, Fig. S7**).

Within each cell, CSs sometimes triggered Ca^{2+} influx in the distal apical dendrites, consistent with prior reports²⁷, but sometimes did not, resulting in a clear bimodal distribution of $\text{Ca}^{2+} \Delta F/F$ amplitude (apical Ca^{2+} transients in $46 \pm 19\%$ of CSs, mean \pm s.d., $n = 399$ events, 23 branches, 10 neurons, **Fig. 2a,b, Fig. S7**). The ratio of the Ca^{2+} signals from CSs (averaged over all CS events) vs. SSs was an increasing function of distance from the soma: in the distal apical dendrites, Ca^{2+} was almost entirely due to CSs (**Fig. 2d,e**). This result indicates that CSs play a privileged role in Ca^{2+} -mediated signaling in distal dendrites²⁷.

We also observed rare voltage and Ca^{2+} events co-localized to individual dendritic branches (dSpikes), without detectable somatic voltage or somatic Ca^{2+} signals ($n = 57$ events in 2 recording hours, 4 out of 12 cells, 4 out of 9 mice, **Fig. 2f, Fig. S8**). The local voltage dSpikes had a wider spatial footprint than the corresponding Ca^{2+} dSpikes (full width at half-maximum for voltage: $107 \pm 40 \mu\text{m}$, Ca^{2+} : $66 \pm 39 \mu\text{m}$, mean \pm s.d., **Fig. S8**). The rate of Ca^{2+} dSpikes was 23-fold lower than that of the somatic Ca^{2+} events ($0.18 \pm 0.14 \text{ Hz}$ vs. $0.008 \pm 0.016 \text{ Hz}$, mean \pm s.d., $n = 12$ cells, **Fig. 2g**). Our results show that dendritic Ca^{2+} follows a hierarchical structure: Ca^{2+} events are almost always largest at the soma, and then extend to varying distances out along the dendritic tree. Dendritic Ca^{2+} in CA2 pyramidal cells appears primarily to indicate spike back-propagation rather than integration.

Small changes in voltage back-propagation lead to large changes in dendritic Ca^{2+}

We next examined the variability in the apical CS voltage and Ca^{2+} signals. **Fig. 3a** illustrates two successive CS events, labeled α and β , which showed opposite Ca^{2+} success and failure patterns in two dendrites, D1 and D2. For each event, the accompanying voltage signal was only slightly larger in the Ca^{2+} -positive branch than in the Ca^{2+} -negative branch. This pattern of branch-specific variations in Ca^{2+} and broadly shared voltage re-occurred across all CS events in the recording (**Fig. 3a-e, Supplementary Videos 2&3**). The Ca^{2+} failures often occurred near branch points (**Fig. 3c,h, Fig. S9**), though the voltage signals decayed smoothly across the branch points (**Fig. 3c,i, Fig. S9**). Similar branch-specific penetration of bAP-triggered Ca^{2+} signals has been observed in both CA1 and cortical pyramidal neurons in brain slices^{15,23,50} and *in vivo*^{28,30,51}. Our data demonstrate substantially stronger branch-specific variation in Ca^{2+} than in voltage *in vivo*.

To quantify this effect, we compared the voltage area-under-the-curve (AUC) and $\text{Ca}^{2+} \Delta F/F$ amplitude at soma and dendrites. Across events with different numbers of spikes and different

subthreshold amplitudes, the voltage AUC was highly correlated between the soma and all dendritic branches (**Fig. 3f,j, Fig. S10**); whereas the correlation between $\text{Ca}^{2+} \Delta F/F$ at soma vs. dendrite decreased sharply at distances $> 200 \mu\text{m}$ (**Fig. 3g,j, Fig. S10**). Similarly, the voltage AUC between pairs of distal apical dendrites from the same cell was also highly correlated, while the pairwise correlation between the corresponding $\text{Ca}^{2+} \Delta F/F$ amplitude was significantly lower (**Fig. 3k**).

A simple biophysics-inspired model relates dendritic voltage and Ca^{2+} *in vivo*

We sought to understand the distinctive spatial structures of voltage and Ca^{2+} during back-propagation. We plotted local $\text{Ca}^{2+} \Delta F/F$ vs. local voltage AUC across diverse somatic spiking events, for different sub-cellular compartments. The voltage-to- Ca^{2+} relation transitioned from sublinear at and near the soma to sigmoidal with an apparent threshold in distal dendrites (**Fig. 4a, Fig. S11**). Prior efforts to model the voltage-to- Ca^{2+} relation aspired to multi-component realistic descriptions^{52,53}, but the visually apparent trends in our data suggested that a simple semi-empirical fit might suffice to capture the physiological dynamics.

We hypothesized that the voltage-to- Ca^{2+} relation might be captured by a family of sigmoidal curves resembling ion channel activation gates. We made a minimal model inspired by voltage-dependent gating of a hypothetical voltage-gated Ca^{2+} channel (VGCC, **Fig. 4b, Methods**)⁵⁴, though we emphasize that this model is not molecularly specific: it seeks to integrate the combined effects of all-voltage-dependent Ca^{2+} conductances, as well as internal Ca^{2+} handling, into a small number of parameters. We described the channel gating by a sigmoidal function $m_\infty(V)$, and assumed that the channel open probability followed $P_{\text{open}} = m^2$ ^{50,55}. This model assumed rapid channel activation and ignored channel inactivation (i.e. no h gate). We assumed a Ca^{2+} influx rate $i_{\text{Ca}^{2+}} \propto P_{\text{open}} \times (E_{\text{Ca}^{2+}} - V(t))$, where $(E_{\text{Ca}^{2+}} - V(t))$ is the driving force for Ca^{2+} influx. Since the voltage events were much faster than the Ca^{2+} events, and the Ca^{2+} upstroke was much faster than the return to baseline, we treated the voltage events as an impulsive Ca^{2+} influx and we did not model Ca^{2+} efflux, i.e. the model converted the function $V(t)$ for each event into a prediction of the peak $\text{Ca}^{2+} \Delta F/F$.

We performed a global fit for $E_{\text{Ca}^{2+}}$ (in units of $\Delta F/F$) and the gating “charge” q (units $(\Delta F/F)^{-1}$), and then held these parameters fixed across all cells and compartments. We then fit two parameters for each subcellular compartment: the ion channel activation threshold V_0 (units of $\Delta F/F$) and an overall scaling factor, A . We performed the fit for $n = 12$ neurons, with 13 – 79 compartments per cell and 12 – 274 events per cell (1225 total events, 476 total compartments, 37,039 total predictions). This simple model successfully predicted Ca^{2+} event amplitudes across all compartments in all cells with $R^2 = 0.88$ (**Fig. 4c,d, Fig. S12**). Saturation of the jGCaMP8m signal at high $[\text{Ca}^{2+}]$ might account for the model’s slight overestimate of $\text{Ca}^{2+} \Delta F/F$ amplitude for the largest events. While we used only the bAPs for parameter fitting, the model also predicted the amplitude of local Ca^{2+} dSpikes from the accompanying local voltage dSpikes (**Fig. S13**).

Though the apparent VGCC activation voltage, V_0 , was fit independently for each dendritic compartment, this parameter showed regular trends across cells. V_0 increased with distance from the soma, in both the apical and basal directions (**Fig. 4e-g**). This trend captured the transition from sub-linear Ca^{2+} response near the soma to sigmoidal and increasingly step-like Ca^{2+} responses in the apical dendrites. The change in shape of the voltage-to- Ca^{2+} transfer function could not be

trivially explained by position-dependent changes in sensitivity of either the voltage or calcium recordings. Rather, this finding implies a gradient toward increasing threshold for activation of Ca^{2+} influx with increasing distance from the soma. While the biophysical basis of this gradient is unknown, we speculate that its functional role may be to prevent activation of Ca^{2+} signaling by weak or incoherent patterns of synaptic inputs.

Our model established a 1:1 deterministic relation between local voltage dynamics and peak local Ca^{2+} in each dendritic segment. In the apical compartments, small differences in voltage were amplified by the steep nonlinear activation of Ca^{2+} channels into large branch-specific variations in Ca^{2+} .

These observations raised the question: what causes the variations in local CS voltage waveforms which appear to drive distal branch-specific Ca^{2+} success or failure? NMDA receptors, which, together with VGCCs, provide the large and sustained apical currents which drive CSs, activate upon conjunction of extracellular glutamate and electrical depolarization from a bAP^{27,43,54}. We thus speculated that the branches which showed larger CS Ca^{2+} signals might have stronger excitatory drive leading up to the first spike in the CS. To test this hypothesis, we quantified the mean subthreshold voltage in each dendritic branch during the 100 ms preceding the first spike in each CS event (pre-AUC), as a proxy for local excitatory drive. We observed a weak, but statistically significant, correlation between pre-AUC and local CS-evoked Ca^{2+} in apical dendrites, but not in the somas (**Fig. S14**). High- Ca^{2+} events showed, on average, a higher pre-AUC compared to low- Ca^{2+} events (high Ca^{2+} : pre-AUC = 0.63 ± 0.33 ; low Ca^{2+} : pre-AUC = 0.04 ± 0.26 , $P = 1.5 \times 10^{-6}$, $n = 256$ events, 17 distal branches, 7 neurons, 6 animals, **Fig. S14, Methods**). Thus, dendrite-specific synaptic inputs appear to locally amplify subsequent CS events, activating local Ca^{2+} influx, consistent with prior measurements in Purkinje cell dendrites³³. This provides a biophysical mechanism for conjunctive Ca^{2+} signaling, and hence plasticity, at the level of dendritic branches.

Discussion

Dendrites must solve a fundamental problem: how to convert the rich but fleeting vocabulary of electrical signals into the slower biochemical language that governs synaptic plasticity. This voltage-to- Ca^{2+} transformation is the critical transduction step that links millisecond-scale neural activity to hours- and days-long changes in connectivity. Yet despite decades of work in reduced preparations, the rules governing this transformation during natural behavior have remained unclear. Here, by simultaneously mapping voltage and Ca^{2+} across the dendritic arbors of CA2 pyramidal neurons in behaving mice, we provide what is, to our knowledge, the first dendrite-wide characterization of this transfer function in a behaving mammal.

Two conclusions emerge. First, in this behavioral context, dendritic Ca^{2+} signals largely reflect the variable penetration of back-propagating action potentials, with complex spikes disproportionately driving distal apical Ca^{2+} . Second, despite the biological complexity of Ca^{2+} handling, local Ca^{2+} transients are accurately captured by a compact, channel-inspired transfer function of the local voltage waveform, providing a quantitative framework for interpreting dendritic Ca^{2+} imaging.

A prevailing model in neuroscience treats dendrites as independent computational subunits capable of generating local computations and plasticity through Ca^{2+} spikes independent of the soma⁵⁶⁻⁵⁹.

Our findings in CA2 provide a stark counterpoint to this view. The rarity of isolated dendritic Ca^{2+} events suggests that, at least in this cell type and our measurement conditions, the dendrites typically do not act as autonomous calculators.

Our data instead support a model of gated back-propagation in which somatic spiking provides a global broadcast to the dendritic arbor, while the dendrite locally determines whether that broadcast is converted into Ca^{2+} influx. In this regime, small bursts (≤ 3 spikes) failed to recruit distal apical Ca^{2+} , implying that the biochemical threshold relevant for distal apical plasticity is typically reached only during sufficiently strong output. Even then, Ca^{2+} recruitment was not uniform: larger bursts preferentially drove dendritic Ca^{2+} in branches exhibiting preceding subthreshold depolarization, consistent with a nonlinear voltage-to- Ca^{2+} transfer that amplifies local pre-burst activity. This result provides *in vivo* validation of classic patch clamp and Ca^{2+} imaging measurements in acute slices⁵⁴.

This architecture offers a biophysical resolution to synaptic credit assignment. The burst serves as an instructive, global “output occurred” signal, but only branches that were electrically primed immediately beforehand cross the Ca^{2+} threshold and receive a durable biochemical trace. In this way, transient, branch-specific synaptic activation is selectively tagged when it contributes to successful spiking output, providing a high-fidelity mechanism for associative, branch-resolved learning without requiring dendrites to generate frequent independent spikes. This view is consistent with theories in which dendritic compartments supply local instructive signals that enable credit assignment across synapses under a global somatic output^{60,61}.

The second central finding of this study is the remarkable accuracy with which a simple biophysics-inspired model—incorporating only local voltage and a distance-dependent channel activation threshold (V_0)—predicts dendritic Ca^{2+} transient amplitudes ($R^2 \approx 0.88$). Our optical system did not resolve individual dendritic spines, or Ca^{2+} events faster than the 24 ms Ca^{2+} camera exposure time. Thus we cannot address whether this relation persists to such small scales of space or time. Nonetheless, this high degree of predictability over the measured scales is surprising, given the diversity of voltage-gated ion channels, neuromodulatory states, and possible amplification by ER-mediated Ca^{2+} release.

Despite the complexity of dendritic Ca^{2+} handling machinery, our results suggest that in the awake, behaving animal, the biophysical state of the dendrite is constrained to a regime where Ca^{2+} influx is a robust and reliable reporter of the local voltage waveform. This robustness is comforting, considering the central role that Ca^{2+} plays in orchestrating downstream biochemical signaling. The distal increase in V_0 likely reflects a mechanism to ensure that only sufficiently robust conjunction of spike back-propagation and synaptic input – sufficient to evoke a dendritic plateau potential – triggers Ca^{2+} influx and plasticity, while subthreshold noise and isolated bAPs do not.

The question remains whether our two key findings – a primacy of back-propagation as a trigger for dendritic Ca^{2+} and a deterministic $V \rightarrow \text{Ca}^{2+}$ transfer function – generalize to other pyramidal neurons such as those in CA1 or the neocortex, and to other brain states or behaviors. CA2 is notably distinct: it is resistant to many forms of long-term potentiation (LTP)^{62–64} and plays a specialized role in social memory³⁴, which requires high stability. It is striking that the conjunctive Ca^{2+} mechanism we identified is localized to the apical dendrites, which is the region of CA2 with

the strongest evidence for activity-dependent plasticity³⁷. It is possible that the lack of isolated dendritic Ca^{2+} events is a specific evolutionary adaptation of CA2 to preserve stable representations of social identity. In contrast, CA1 neurons, which are more plastic, may operate in a high-plasticity regime where isolated Ca^{2+} spikes are more frequent, as has been reported recently³¹.

The optical and molecular tools introduced here are well suited to address these questions, by probing the structures of dendritic excitations across brain regions, cell types, and behavioral settings (e.g. during place-field formation in CA1). The optical system could also be applied to study joint dynamics of membrane voltage and other signals for which there are GFP-based reporters, such as glutamate⁶⁵, GABA⁶⁶, neuromodulators⁶⁷, or other intracellular signaling molecules⁶⁸. Such measurements could further illuminate the rich interplay of electrical and chemical signaling in neurons.

Acknowledgements

We thank Andrew Preecha and Camila Bodden for technical assistance. We thank Liam Paninski, Benjamin Antin, Utku Ferah, Chase King, Amol Pasarkar, Ahmed Abdelfattah, and Eric Salter for helpful discussions. XW acknowledges support from an American Heart Association (AHA) postdoctoral fellowship. BHL acknowledges support from National Research Foundation of Korea (NRF) grant RS-2023-00248959. LDL was supported by the Howard Hughes Medical Institute. This work was supported by a Vannevar Bush Faculty Fellowship N00014-18-1-2859, the Harvard Brain Initiative, NIH grants R01-NS126043, R01-NS133755, and R01-MH117042, and Chan Zuckerberg Initiative Dynamic Imaging Grant 2023-321177.

Author contributions

XW designed the project, developed the optical system, performed animal surgeries and imaging experiments, analyzed data, and wrote the manuscript. BHL developed the genetic construct, optimized the protocol for virus injection and prism implantation surgeries, built the VR system, performed imaging experiments, and analyzed data. PP developed the genetic construct and helped with the experimental design. JDW-C helped with optical system design and data analysis. JX performed histology experiments. SEP and LDL synthesized and provided JF608-HTL. AEC supervised the project and wrote the manuscript. All authors commented on the manuscript.

Competing interests

AEC is a consultant to Quiver Biosciences and to Exin Therapeutics, and is a founder of Luminos LLC. LDL is a scientific cofounder, shareholder, and consultant of Eikon Therapeutics. US Patent 9,933,417 describing azetidine-containing fluorophores and variant compositions (with inventor LDL) is assigned to HHMI. All other authors declare no competing interests.

Data availability

Data are available from the corresponding author upon request.

Supplementary Video captions

Supplementary Video 1. Ca^{2+} and voltage ΔF movies and $\Delta F/F$ traces. Top left: Normalized $\text{Ca}^{2+} \Delta F$, linearly interpolated to 1 kHz. Bottom left: Normalized voltage ΔF . Top right: Real-time somatic $\text{Ca}^{2+} \Delta F/F$ waveform. Bottom right: Real-time somatic voltage $\Delta F/F$ waveform.

Supplementary Video 2. Spatial profile of all Ca^{2+} and voltage events in a representative cell. Top: Ca^{2+} ; bottom: voltage. Inset at the bottom left of the voltage panel shows the somatic voltage waveform of the corresponding event. Events were sorted from lowest to highest somatic $\text{Ca}^{2+} \Delta F/F$.

Supplementary Video 3. Normalized spatial profile of all Ca^{2+} and voltage events in a representative cell. Same data and arrangement as Supplementary Video 2. Each event was normalized by the value in the soma, to highlight the changes in spatial profile.

Methods

Microscope system

The structured illumination spinning disk confocal microscope (**Fig. 1a**, **Fig. S1**) used a 488-nm laser (Coherent, Genesis, MX488, 3W) and a 607-nm laser (Opto Engine LLC, MLL-FN-607, 600 mW) for excitation. A half-wave plate on a rotation mount and a polarizing beam splitter were used to adjust the laser power. The two lasers were combined using a dichroic mirror (IDEX, FF506-Di03-25x36) and coupled into an acousto-optic tunable filter (AOTF, Gooch & Housego, TF525-250-6-3-GH18A) for dynamic modulation of the laser intensity at each wavelength. The two lasers were then separated using another dichroic mirror (IDEX, FF506-Di03-25x36). The 488-nm and 607-nm laser beams were separately expanded by 4 \times and 8 \times telescope systems, respectively. The two lasers were then sent to two digital micromirror devices (DMDs, Vialux, V-7000) for patterned illumination. The DMDs were mounted at a 45° angle relative to the ground, so that the diffracted light stayed in the same horizontal plane as the incident light. The patterned light from each DMD was collected by a separate 4f system, each consisting of two 400-mm convex lenses. Only the central diffraction order was collected. The two lasers were then merged using another dichroic mirror (IDEX, FF506-Di03-25x36).

In commercial spinning disk microscopes, illumination enters through a single-mode optical fiber and is internally homogenized and conveyed onto the spinning disk microlens array. To enable projection of patterned illumination onto the microlens array, we replaced a turning mirror in the side of the spinning disk unit (Yokogawa, CSU-X1) with an optical window in a custom mount (Thorlabs, BCP43R; **Fig. S1b**). The patterned illumination entered through the side window and was re-imaged onto the spinning disk microlens array. The microlens array focused the excitation onto the pinhole array.

An infinity-corrected homebuilt microscope comprised a 100-mm tube lens (TL, Thorlabs, TTL100-A) and a 10 \times objective (Olympus, XLPLN10XSVMP) to achieve an effective magnification of 5.6 \times . The microscope re-imaged the spinning disk pinhole array onto the sample. The fluorescence emission from the sample was collected by the same objective-TL pair and re-imaged onto the pinhole array, to achieve optical sectioning. The fluorescence was then reflected by a custom dichroic mirror (Chroma, zt488/607tpc, 13 \times 15 \times 0.5 mm) between the pinhole array

and the microlens array. After passing through the spinning disk unit, the two-channel emission light was separated by a dichroic mirror (IDEK, FF580-FDi02-t3-25x36). The green (jGCaMP8m) and red (Voltron2-JF608) emission light was cleaned using separate emission filters (Chroma, ET535/70m for green; IDEK, FF01-709/167-25 for red), and re-imaged onto two scientific CMOS cameras (Hamamatsu, ORCA-Fusion, C11440-22CU) using two separate 100-mm lenses (Thorlabs, AC508-100-A-ML).

The voltage-imaging camera row clock (100 kHz, Hsync) was routed to a data acquisition system (DAQ, National Instruments, PCIe-6323) and used as the master clock for imaging experiments. The Luminos software⁴⁰ was used to coordinate the timing and data acquisition during the experiment and to determine the precise spatial mapping of pixels on each DMD to pixels on the respective camera. To synchronize the voltage-imaging camera exposures with the spinning disk rotation, we used the camera frame clock (1 kHz, Vsync) to trigger a high-quality pulse train from a function generator (Tektronix, AFG3102). The output from the function generator was then connected to the CSU_SYNC (Pin No.12 of the PCR68 connector) port of the spinning disk control unit (**Fig. S2a**). It was necessary to use the function generator, since the Vsync signals from the camera had low duty cycle and slow rise time that resulted in unstable rotation speed of the spinning disk. After starting the camera and spinning disk, we waited 2 s before starting data acquisition, to give the spinning disk time to stabilize its rotation speed. The frame clocks from both cameras were sent to the DAQ to precisely align the timing of the two cameras in post-processing.

Genetic Construct

The reporter construct, pAAV-hSyn-DIO-Voltron2-LR-p2A-jGCaMP8m (Addgene #251709), was constructed using standard cloning techniques and confirmed via sequencing (Plasmidsaurus). This construct was packaged into AAV 2/9 by UNC NeuroTools core. The AAV9.CamKII 0.4.Cre.SV40 was a gift from James M. Wilson (Addgene viral prep #105558-AAV9).

Vertebrate animal subjects

All experiments were performed in adult C57BL/6J mice (male, 5-7 weeks old, Jackson Laboratory). All procedures involving animals were in accordance with the National Institutes of Health Guide for the Care and Use of Laboratory Animals and were approved by the Harvard University Institutional Animal Care and Use Committee (IACUC). Animals were group-housed on a reverse 12 h light:12 h dark cycle and had access to food and water *ad libitum*, except during training for and execution of VR experiments when the mice were water restricted, as described below.

Virus injections

The protocol of virus injections was extensively described in Ref. ⁴⁹. In brief, mice were administered dexamethasone (4.8 mg/kg), carprofen (5 mg/kg) and Etiqa XR (3.25 mg/kg) ~1h before the surgery via subcutaneous injection. Mice were then anesthetized with isoflurane and positioned in a stereotaxic frame (Stoelting) with a homeothermic heating pad underneath set at 37 °C. Scalp hair was removed using Nair, and the scalp was disinfected with 70% ethanol and iodine. A scalp incision was made to expose the cranial bone. Three \varnothing 0.5-mm burr holes were made at the stereotaxic coordinates of AP: -1.4 mm, -2.1 mm, -2.8 mm; ML: -1.6 mm using a dental drill (Marathon). The glass micropipettes used for injections were prepared using a Sutter

P1000 puller. A microinjection pump (World Precision Instruments, Nanoliter 2010) was used for loading and injecting the virus. The virus mixture comprising AAV2/9-hSyn-DIO-Voltron2-LR-p2A-jGCaMP8m (final concentration: $1-2 \times 10^{12}$ GC/mL) and AAV9.CamKII 0.4.Cre.SV40 (final concentration: $2-4 \times 10^7$ GC/mL) was injected at all three craniotomy sites at four depths per site (DV: -1.3 mm, -1.2 mm, -1.1 mm, and -1 mm) at a speed of 84 nL/min. 40 nL of virus mixture was injected at each depth, resulting in a total volume of 160 nL per site and 480 nL per animal. After the injection, the scalp was sealed back using Vetbond tissue adhesive (3M). The animal was returned to its home cage with a 37 °C heating pad underneath. The animal's activity was monitored until full recovery from the anesthesia. Carprofen (5 mg/kg) was administrated via subcutaneous injection for 3 days after the surgery.

Prism implantation

The prism (2.5 mm height with a 1.5×1.5 mm square top surface; 45° surface coated by aluminum; Tower Optical)⁴⁵ was attached to a 5-mm glass coverslip using optical adhesive (Norland, NOA81). The adhesive was cured by 10-min of UV illumination. The protocol of prism implantation was adapted from Ref. ⁴⁵ and was extensively described in Ref. ⁴⁹. Briefly, the prism implantation surgery was performed 1 week after the AAV injections. The initial procedures up to scalp incision were the same as in **Virus Injections** above. After cranial bone exposure, a 0.5×1.5 mm craniotomy was created using a dental drill centered around the 3 virus injection sites. A single-edge diamond knife (Fisher Scientific, 501930985) was slowly inserted (1 mm/min) through the craniotomy to create a vertical incision with a depth of 1.5-2 mm. The diamond knife was extracted at the same speed to minimize bleeding. Afterwards, a \varnothing 3-mm craniotomy surrounding the diamond knife incision was created using a biopsy punch and a dental drill. The dura mater within the craniotomy was carefully removed using a fine forceps and a Bonn Micro Probe (Fine Science Tools), and the exposed brain was covered by sterile saline. The prism was attached to a blunt-end 14-gauge needle with vacuum and aligned with the incision created by the diamond knife. The prism was then slowly lowered (1 mm/min) inside the incision until the top coverslip was in contact with the skull. During the prism insertion, the side interface of the prism was carefully monitored through the top to ensure that the hippocampal structures (including CA1, CA3, and DG) could be clearly seen. The top coverslip was then fixed on the skull using Vetbond tissue adhesive (3M) and dental cement (Parkell, C&B metabond, 242-3200). Last, a stainless steel headplate was attached to the skull using dental cement. The post-operative procedures were the same as the ones described in **Virus Injections** above.

Virtual reality (VR) system and training

The VR system was adapted from the design by Christopher Harvey lab (<https://github.com/HarveyLab/mouseVR>) and the VR environment was designed using the ViRMEn software (<https://pni.princeton.edu/pni-software-tools/virmen>). Mice were put under water restriction for 3 days (1 mL of water per day) and were trained to run on the VR system for water reward. Animals running more than 50 m in 30 min were considered ready for imaging, typically after 10-14 days of training. The details of the VR system hardware and training procedures were extensively described in Ref. ⁴⁹.

Image acquisition

Mice were allowed to recover for at least 8 weeks from the prism implantation surgery before imaging. The day before the imaging session, we prepared 100 μ L of 0.5 mM JF608-HaloTag

solution by dissolving 50 nmol of JF608 powder in 10 μ L of DMSO, 10 μ L of Pluronic F-127 (20% w/v in DMSO), and 80 μ L of 1 \times PBS. The JF608-HaloTag solution was then delivered via retro-orbital injection at least 12 h before imaging. During the imaging session, the animal was head-fixed and positioned on the treadmill of the VR system. After a target neuron was identified, the mouse and VR system were translated to position the neuron at the center of the field of view. A reference image was acquired and used to manually define DMD patterns for targeted illumination. 60-90 mW/mm² 607-nm light and 5-8 mW/mm² 488-nm light were delivered for illumination. The voltage recording was acquired at 1 kHz and the Ca²⁺ recording was acquired at 41.5 Hz.

After the functional recording, a 25 \times objective (Olympus, XLPLN25XSVMP2) was put onto the spinning disk confocal microscope to acquire a high-resolution z-stack image of the neuron structure (0.5- μ m axial spacing). Multiple z-stacks were stitched together using the Pairwise Stitching plug-in in Fiji ImageJ. The dendrite tracing was performed on the stitched z-stack image using the Simple Neurite Tracer (SNT)⁶⁹ plug-in in Fiji ImageJ.

Image processing

All data analysis was performed in MATLAB. **Fig. S3** provides an overview of the pipeline.

Spinning disk sector correction

The Nipkow spinning disk pinhole array comprised twelve nominally identical sectors, i.e. one revolution of the disk provided twelve scans of the field of view. The voltage-imaging camera acquired one image per sector (twelve per disk revolution). We found that slight variations between the twelve sectors led to period-twelve noise in the voltage-imaging data (**Fig. S2**). We corrected this noise in post-processing, as follows. The temporal average of all frames was used as a reference image. The raw data were then separated into twelve groups based on the remainder after dividing the frame index by twelve (e.g. Group 1: Frames 1, 13, 25...; Group 2: Frames 2, 14, 26...). All frames within each group were averaged, and this average image was divided by the reference image to calculate a group-specific correction pattern. This correction pattern was then divided from all the frames in the corresponding group, and the images from all groups were re-interleaved to reconstruct the corrected data.

This artifact did not occur in the Ca²⁺ imaging data because the frame-rate of the Ca²⁺ camera (41.5 Hz) averaged over two complete rotations of the disk for each frame.

Voltage and Ca²⁺ image registration

We first obtained the time-average images from the voltage and Ca²⁺ recordings as reference images. We manually selected >15 pairs of control points in each channel, using the *cpselect* function in MATLAB. We then used the *fitgeotform2d* function in MATLAB to calculate an affine transformation to map the Ca²⁺ reference image to the voltage reference image. Once the mapping was visually confirmed to be accurate, the transformation was applied to all the frames in the Ca²⁺ recording.

Voltage signal extraction

We corrected the sample motion using NoRMCorre⁷⁰. To identify pixels contaminated by blood vessels, we calculated the lag-1 autocorrection image as $C(x, y) = \langle \Delta F(x, y, n) \cdot \Delta F(x, y, n + 1) \rangle$

$1\rangle\rangle_n$, where n is the frame index and $\langle\cdot\rangle_n$ is the average over all frames. Pixels contaminated by blood vessels were highlighted in this image and were manually masked^{44,49}. We then manually selected ROIs (20-30 μm in length) in the soma and along each dendrite.

To correct for photobleaching, we first did a rough spike detection and defined silent periods without spiking events. We then obtained the average intensity of all pixels for the silent periods and fitted a two-component exponential decay as an estimate of the bleaching baseline. This bleaching baseline was then divided from the entire recording. We removed residual motion by regressing out the motion traces ($x(t)$, $y(t)$, $x^2(t)$, $y^2(t)$, and $x(t) \cdot y(t)$ provided by the NoRMCorre algorithm) from the movie.

For each ROI, we performed principal component analysis (PCA) to obtain the voltage footprint (Fig. S3c)^{44,49}. Usually the first principal component (PC) had a spatial footprint that matched the structure of the dendrite, and a corresponding time trace which clearly represented voltage dynamics. Other PCs showed spatial structures that indicated residual noise, including sample motion, blood-flow artifacts, animal breathing, and shot noise. We corrected for residual baseline drift by subtracting a low-pass-filtered version of the trace (5-s moving average). Last, we divided by the median value of the low-pass-filtered trace to determine raw $\Delta F/F$ voltage dynamics at each ROI.

Voltage spike detection and classification

The raw voltage $\Delta F/F$ trace was high-pass-filtered by subtracting a 50-ms moving-median trace. We then used the *findpeaks* function in MATLAB with a threshold z-score of 5 to detect voltage spikes in each ROI. Spikes with ≤ 1 ms difference in peak timing in neighboring ROIs were linked to the same event. Successive spikes with ≤ 25 ms inter-spike interval at the soma were considered part of the same bursting event. Dendritic spikes without a somatic spike within 4 ms were defined as local voltage dSpikes. We manually examined the raw ΔF movies for all the identified voltage dSpikes to ensure classification accuracy.

Complex spikes (CS) were defined as bursts comprising 4 or more spikes, accompanied by a sufficiently large subthreshold depolarization. To obtain the subthreshold voltages, three frames before and after each spike were removed, and the missing data were filled using linear interpolation. The resulting trace was low-pass-filtered with a 20-ms moving average. Subthreshold depolarizations with peak amplitude exceeding a z-score of 5 (~50% of the spike amplitude) were considered above-threshold for a CS. All the identified CS events were manually examined to ensure classification accuracy.

The first and last frames of a CS were defined as the points where the rising and falling edges of the depolarization bump crossed a z-score of 1.5. For all non-CS bursts, the duration was defined as 5 frames before the first spike to 5 frames after the last spike. For local voltage dSpikes, the duration was defined as the interval between the two local minima around the peak when the voltage was below a z-score of 1.5. The voltage area under the curve (AUC) was calculated by integrating all frames within the duration of each event.

Ca^{2+} signal extraction

The Ca^{2+} camera exposure was 24-fold slower than the voltage camera exposure, so there was no need to apply the disk sector correction. We first applied the NoRMCorre motion correction and photobleaching correction as described above. The Ca^{2+} recording was spatially registered to the voltage recording, as described above. We then extracted the raw Ca^{2+} intensity traces using the same ROIs as for the voltage. We estimated slow baseline fluctuations using the *smooth* function in MATLAB (“rlowess” smoothing method with a 100-frame, 2.4 second, smoothing window). This method assigns lower weight to outliers and thus preserves the Ca^{2+} transient peaks. We also manually examined the raw Ca^{2+} intensity traces and the fitted smooth baseline from all ROIs to ensure the preservation of Ca^{2+} spikes. The smoothed baseline was subtracted from the raw traces, and division by the median value of the smoothed baseline resulted in the raw Ca^{2+} $\Delta\text{F}/\text{F}$ dynamics at each ROI.

Ca^{2+} spike detection and classification

We used the *findpeaks* function in MATLAB with a threshold z-score of 3 ($\sim 5\%$ raw $\Delta\text{F}/\text{F}$) to detect Ca^{2+} spikes. Dendritic Ca^{2+} events without somatic Ca^{2+} within 2 frames were classified as local Ca^{2+} dSpikes. We manually examined the raw ΔF movies for all the identified Ca^{2+} dSpikes to ensure classification accuracy. For each Ca^{2+} spike, we identified the corresponding voltage dynamics.

For each ROI, the amplitudes of Ca^{2+} spikes were calculated by taking the average of the two largest frames around the peak frame. Negative event amplitude was replaced with 0. Sometimes a Ca^{2+} spike happened on top of the tail of the preceding Ca^{2+} spike. In this case, we calculated the ratio between the minimum in the decaying tail of the earlier event and the maximum of the later event. When this ratio was ≥ 0.3 , the later event was excluded from analysis. Otherwise, an exponential decay curve was fitted to the decaying tail of the previous event and extrapolated to the time of the peak of the later event. This exponential fit was then subtracted from the later event before calculating event amplitude.

Calculating “Robust $\Delta\text{F}/\text{F}$ ”

For both voltage and Ca^{2+} , each ROI may have different levels of background, which affect raw $\Delta\text{F}/\text{F}$. To make the $\Delta\text{F}/\text{F}$ values comparable across cells and ROIs, we performed robust estimation of $\Delta\text{F}/\text{F}$, as shown in **Fig. S3d** and elaborated in Refs. ^{44,50}. In brief, for each cell, we calculated the spike-triggered-average (STA) movie of all CS events. For voltage, all events were aligned to the first spike inside the CS, and we took the temporal average of the STA movie to obtain a voltage CS ΔF image. For Ca^{2+} , all events were aligned to the peak frame, and we averaged 3 frames centered around the peak frame to obtain a Ca^{2+} CS ΔF image. We also calculated F_0 images for voltage and Ca^{2+} by taking the temporal average of all silent periods (i.e. no voltage or Ca^{2+} spiking events). For each ROI, we made a pixel-by-pixel scatter plot of ΔF vs. F_0 . We calculated a linear regression for this scatter plot, and the slope of the fitted line represented the robust $\Delta\text{F}/\text{F}$ of CS STA for that ROI (i.e. $\partial\Delta\text{F}/\partial\text{F}_0$). Any spatially homogenous background signal within the ROI only resulted in an offset of the F_0 values and did not affect the slope. We also took the average of the same time window for the raw $\Delta\text{F}/\text{F}$ traces to obtain the raw $\Delta\text{F}/\text{F}$ of CS STA. The ratio between $\partial\Delta\text{F}/\partial\text{F}_0$ and raw $\Delta\text{F}/\text{F}$ of CS STA provided a scaling factor for each ROI. This scaling factor was then multiplied to the raw $\Delta\text{F}/\text{F}$ traces to obtain the robust $\Delta\text{F}/\text{F}$ traces. This robust $\Delta\text{F}/\text{F}$ scaling was calculated separately for each voltage and Ca^{2+} trace in each ROI.

Biophysical characteristics of SS back-propagation

For each cell, we obtained a SS STA voltage trace for all ROIs. We then did a cubic spline interpolation to find the amplitude and timing of the peak in each ROI. For Ca^{2+} , we calculated the average amplitude of all SS-induced Ca^{2+} events for each ROI. Within each cell, the peak amplitudes as a function of contour distance from the soma were fit with a single exponential decay curve. This provided voltage and Ca^{2+} SS decay length constants for each cell. To obtain the voltage back-propagation speed, we plotted the SS voltage delay vs. contour distance for all ROIs. We then fitted a line for ROIs $\leq 250\text{-}\mu\text{m}$ away from soma, and the inverse of the slope was the propagation speed.

Pre-spike voltage AUC for high vs. low Ca^{2+} events in distal dendrite

We first selected ROIs that were $\geq 300\text{-}\mu\text{m}$ from the soma. ROIs within the same dendritic branch were combined. For all CS-induced Ca^{2+} events in the soma, we calculated the corresponding Ca^{2+} event amplitude in each distal dendrite using the method described above. We calculated the average amplitude of the largest 5 events and used 50% of this value as the threshold to classify high- Ca^{2+} events and low- Ca^{2+} events. Within each category, we identified the corresponding voltage events and aligned them in time to the first spike in the soma. Events that happened within 100 ms after the previous events were excluded. All remaining voltage events within the same category were averaged to obtain a high- Ca^{2+} and a low- Ca^{2+} voltage STA trace for each branch. This procedure was then repeated across all distal branches. The pre-spike voltage AUC was calculated by integrating the -100 to -2 ms time window before the first spike in the soma.

Biophysics-inspired voltage-to- Ca^{2+} model

We estimated the value of $E_{\text{Ca}^{2+}}$ (0.45 in the unit of robust $\Delta F/F$) from the Ca^{2+} equilibrium potential (132 mV with a 2×10^4 -fold difference in extracellular vs. intracellular $[\text{Ca}^{2+}]$) and the voltage sensitivity calibration curve of Voltron2-JF608 in Ref. ⁴³. The value of q (60 in the unit of reciprocal robust $\Delta F/F$) was estimated based on the activation curves of voltage-gated Ca^{2+} channels^{55,71–73} and the same calibration curve of Voltron2-JF608. The values of $E_{\text{Ca}^{2+}}$ and q were fixed across all cells and all ROIs. For each ROI, all pairs of voltage event traces and Ca^{2+} event amplitude were used to fit the scaling factor A and the activation threshold V_0 by using the *lsqcurvefit* function in MATLAB. A lower bound of 0 was set for V_0 fitting.

Histology

Mice were transcardially perfused with 1× PBS followed by 4% paraformaldehyde (PFA). The brain was dissected from the skull and post-fixed in 4% PFA at 4 °C for 24 h. 40 μm coronal sections were collected using a vibratome (Leica VT1200S). The brain slices were then rinsed at room temperature with 1× PBS three times for 10 min each, and then blocked for 1 h at room temperature using a blocking solution consisting of 5% bovine serum albumin (BSA) and 1% Triton X-100 in 1× PBS. The brain slices were then incubated with a rabbit anti-GFAP primary antibody (1:500 dilution, Abcam, ab7260) with 1% BSA and 1% Triton X-100 in 1× PBS for 24 h at room temperature. After primary antibody incubation, the brain slices were washed three times with 10 min each at room temperature, with 1% Triton X-100 in 1× PBS. The slices were then incubated with a goat anti-rabbit, Alexa Fluor 488 secondary antibody (1:500 dilution, Invitrogen, A-11008) with 1% BSA and 1% Triton X-100 in 1× PBS for 2 h at room temperature. After secondary antibody incubation, the brain slices were washed in 1× PBS with 1% Triton X-100 three times for 10 min each at room temperature. Afterwards, the slices were mounted onto a glass

slide with an antifade mounting medium (Vector Laboratories, H-1900-2). The mounted slides were imaged using a Zeiss Axio Scan.Z1 epifluorescence microscope.

References

1. Golding, N. L., Staff, N. P. & Spruston, N. Dendritic spikes as a mechanism for cooperative long-term potentiation. *Nature* **418**, 326–331 (2002).
2. Mateos-Aparicio, P. & Rodríguez-Moreno, A. Calcium Dynamics and Synaptic Plasticity. in *Calcium Signaling* (ed. Islam, Md. S.) 965–984 (Springer International Publishing, 2020).
3. Stuart, G. J. & Spruston, N. Dendritic integration: 60 years of progress. *Nat. Neurosci.* **18**, 1713–1721 (2015).
4. Spruston, N. Pyramidal neurons: dendritic structure and synaptic integration. *Nat. Rev. Neurosci.* **9**, 206–221 (2008).
5. Häusser, M., Spruston, N. & Stuart, G. J. Diversity and Dynamics of Dendritic Signaling. *Science* **290**, 739–744 (2000).
6. London, M. & Häusser, M. Dendritic Computation. *Annu. Rev. Neurosci.* **28** 503–532 (2005).
7. Magee, J. C. Dendritic integration of excitatory synaptic input. *Nat. Rev. Neurosci.* **1**, 181–190 (2000).
8. Ohno-Shosaku, T. & Kano, M. Endocannabinoid-mediated retrograde modulation of synaptic transmission. *Curr. Opin. Neurobiol.* **29**, 1–8 (2014).
9. Verma, M., Lizama, B. N. & Chu, C. T. Excitotoxicity, calcium and mitochondria: a triad in synaptic neurodegeneration. *Transl. Neurodegener.* **11**, 3 (2022).
10. Svoboda, K., Denk, W., Kleinfeld, D. & Tank, D. W. In vivo dendritic calcium dynamics in neocortical pyramidal neurons. *Nature* **385**, 161–165 (1997).
11. Svoboda, K., Helmchen, F., Denk, W. & Tank, D. W. Spread of dendritic excitation in layer 2/3 pyramidal neurons in rat barrel cortex in vivo. *Nat. Neurosci.* **2**, 65–73 (1999).
12. Beaulieu-Laroche, L., Toloza, E. H. S., Brown, N. J. & Harnett, M. T. Widespread and Highly Correlated Somato-dendritic Activity in Cortical Layer 5 Neurons. *Neuron* **103**, 235–241.e4 (2019).
13. Takahashi, N., Oertner, T. G., Hegemann, P. & Larkum, M. E. Active cortical dendrites modulate perception. *Science* **354**, 1587–1590 (2016).
14. Jain, A. *et al.* Dendritic, delayed, stochastic CaMKII activation in behavioural time scale plasticity. *Nature* **635**, 151–159 (2024).
15. Spruston, N., Schiller, Y., Stuart, G. & Sakmann, B. Activity-Dependent Action Potential Invasion and Calcium Influx into Hippocampal CA1 Dendrites. *Science* **268**, 297–300 (1995).
16. Regehr, W. G. & Tank, D. W. Postsynaptic NMDA receptor-mediated calcium accumulation in hippocampal CA1 pyramidal cell dendrites. *Nature* **345**, 807–810 (1990).
17. Yuan, L.-L. & Chen, X. Diversity of potassium channels in neuronal dendrites. *Prog. Neurobiol.* **78**, 374–389 (2006).
18. Frick, A. & Johnston, D. Plasticity of dendritic excitability. *J. Neurobiol.* **64**, 100–115 (2005).
19. Rizzuto, R., De Stefani, D., Raffaello, A. & Mammucari, C. Mitochondria as sensors and regulators of calcium signalling. *Nat. Rev. Mol. Cell Biol.* **13**, 566–578 (2012).
20. O’Hare, J. K. *et al.* Compartment-specific tuning of dendritic feature selectivity by intracellular Ca²⁺ release. *Science* **375**, eabm1670 (2022).
21. Jaffe, D. B. *et al.* The spread of Na⁺ spikes determines the pattern of dendritic Ca²⁺ entry into hippocampal neurons. *Nature* **357**, 244–246 (1992).
22. Stuart, G. J. & Sakmann, B. Active propagation of somatic action potentials into neocortical pyramidal cell dendrites. *Nature* **367**, 69–72 (1994).
23. Short, S. M. *et al.* The stochastic nature of action potential backpropagation in apical tuft dendrites. *J. Neurophysiol.* **118**, 1394–1414 (2017).

24. Magee, J. C. *et al.* Subthreshold synaptic activation of voltage-gated Ca²⁺ channels mediates a localized Ca²⁺ influx into the dendrites of hippocampal pyramidal neurons. *J. Neurophysiol.* **74**, 1335–1342 (1995).
25. Schiller, J., Major, G., Koester, H. J. & Schiller, Y. NMDA spikes in basal dendrites of cortical pyramidal neurons. *Nature* **404**, 285–289 (2000).
26. Helmchen, F., Svoboda, K., Denk, W. & Tank, D. W. In vivo dendritic calcium dynamics in deep-layer cortical pyramidal neurons. *Nat. Neurosci.* **2**, 989–996 (1999).
27. Grienberger, C., Chen, X. & Konnerth, A. NMDA Receptor-Dependent Multidendrite Ca²⁺ Spikes Required for Hippocampal Burst Firing In Vivo. *Neuron* **81**, 1274–1281 (2014).
28. Otor, Y. *et al.* Dynamic compartmental computations in tuft dendrites of layer 5 neurons during motor behavior. *Science* **376**, 267–275 (2022).
29. Sheffield, M. E. J. & Dombeck, D. A. Calcium transient prevalence across the dendritic arbor predicts place field properties. *Nature* **517**, 200–204 (2015).
30. Sheffield, M. E. J., Adoff, M. D. & Dombeck, D. A. Increased Prevalence of Calcium Transients across the Dendritic Arbor during Place Field Formation. *Neuron* **96**, 490–504.e5 (2017).
31. O’Hare, J. K., Wang, J., Shala, M. D., Polleux, F. & Losonczy, A. Distal tuft dendrites predict properties of new hippocampal place fields. *Neuron* **113**, 1969–1982.e7 (2025).
32. Roome, C. J. & Kuhn, B. Simultaneous dendritic voltage and calcium imaging and somatic recording from Purkinje neurons in awake mice. *Nat. Commun.* **9**, 3388 (2018).
33. Roome, C. J. & Kuhn, B. Dendritic coincidence detection in Purkinje neurons of awake mice. *eLife* **9**, e59619 (2020).
34. Hitti, F. L. & Siegelbaum, S. A. The hippocampal CA2 region is essential for social memory. *Nature* **508**, 88–92 (2014).
35. Piskorowski, R. A. & Chevaleyre, V. Synaptic integration by different dendritic compartments of hippocampal CA1 and CA2 pyramidal neurons. *Cell. Mol. Life Sci.* **69**, 75–88 (2012).
36. Srinivas, K. V. *et al.* The Dendrites of CA2 and CA1 Pyramidal Neurons Differentially Regulate Information Flow in the Cortico-Hippocampal Circuit. *J. Neurosci.* **37**, 3276–3293 (2017).
37. Chevaleyre, V. & Siegelbaum, S. A. Strong CA2 Pyramidal Neuron Synapses Define a Powerful Disynaptic Cortico-Hippocampal Loop. *Neuron* **66**, 560–572 (2010).
38. Xiao, S. *et al.* Large-scale deep tissue voltage imaging with targeted-illumination confocal microscopy. *Nat. Methods* **21**, 1094–1102 (2024).
39. Qin, S., Isbaner, S., Gregor, I. & Enderlein, J. Doubling the resolution of a confocal spinning-disk microscope using image scanning microscopy. *Nat. Protoc.* **16**, 164–181 (2021).
40. Itkis, D. G. *et al.* Luminos: open-source software for bidirectional microscopy. *bioRxiv* 2025.02.22.639658 (2025).
41. Abdelfattah, A. S. *et al.* Sensitivity optimization of a rhodopsin-based fluorescent voltage indicator. *Neuron* **111**, 1547–1563.e9 (2023).
42. Zhang, Y. *et al.* Fast and sensitive GCaMP calcium indicators for imaging neural populations. *Nature* **615**, 884–891 (2023).
43. Park, P. *et al.* Dendritic excitations govern back-propagation via a spike-rate accelerometer. *Nat. Commun.* **16**, 1333 (2025).
44. Wong-Campos, J. D. *et al.* Voltage dynamics of dendritic integration and back-propagation in vivo. *bioRxiv* 2023.05.25.542363 (2023).

45. Redman, W. T. *et al.* Long-term transverse imaging of the hippocampus with glass microscopes. *eLife* **11**, e75391 (2022).
46. Dudek, S. M., Alexander, G. M. & Farris, S. Rediscovering area CA2: unique properties and functions. *Nat. Rev. Neurosci.* **17**, 89–102 (2016).
47. Chia, T. H. & Levene, M. J. Microprisms for In Vivo Multilayer Cortical Imaging. *J. Neurophysiol.* **102**, 1310–1314 (2009).
48. Andermann, M. L. *et al.* Chronic cellular imaging of entire cortical columns in awake mice using microprisms. *Neuron* **80**, 900–913 (2013).
49. Lee, B. H. *et al.* Dendritic excitations primarily mediate back-propagation in CA1 pyramidal neurons during behavior. *bioRxiv* 2026.01.03.696606 (2026).
50. Landau, A. T. *et al.* Dendritic branch structure compartmentalizes voltage-dependent calcium influx in cortical layer 2/3 pyramidal cells. *eLife* **11**, e76993 (2022).
51. Francioni, V., Padamsey, Z. & Rochefort, N. L. High and asymmetric somato-dendritic coupling of V1 layer 5 neurons independent of visual stimulation and locomotion. *eLife* **8**, e49145 (2019).
52. Jaffe, D. B. *et al.* A model for dendritic Ca^{2+} accumulation in hippocampal pyramidal neurons based on fluorescence imaging measurements. *J. Neurophysiol.* **71**, 1065–1077 (1994).
53. Magee, J., Hoffman, D., Colbert, C. & Johnston, D. Electrical and calcium signaling in dendrites of hippocampal pyramidal neurons. *Annu. Rev. Physiol.* **60**, 327–346 (1998).
54. Magee, J. C. & Johnston, D. A Synaptically Controlled, Associative Signal for Hebbian Plasticity in Hippocampal Neurons. *Science* **275**, 209–213 (1997).
55. Reuveni, I., Friedman, A., Amitai, Y. & Gutnick, M. Stepwise repolarization from Ca^{2+} plateaus in neocortical pyramidal cells: evidence for nonhomogeneous distribution of HVA Ca^{2+} channels in dendrites. *J. Neurosci.* **13**, 4609–4621 (1993).
56. Poirazi, P., Brannon, T. & Mel, B. W. Pyramidal Neuron as Two-Layer Neural Network. *Neuron* **37**, 989–999 (2003).
57. Polksy, A., Mel, B. W. & Schiller, J. Computational subunits in thin dendrites of pyramidal cells. *Nat. Neurosci.* **7**, 621–627 (2004).
58. Beniaguev, D., Segev, I. & London, M. Single cortical neurons as deep artificial neural networks. *Neuron* **109**, 2727–2739.e3 (2021).
59. Boahen, K. Dendrocentric learning for synthetic intelligence. *Nature* **612**, 43–50 (2022).
60. Urbanczik, R. & Senn, W. Learning by the Dendritic Prediction of Somatic Spiking. *Neuron* **81**, 521–528 (2014).
61. Guerguiev, J., Lillicrap, T. P. & Richards, B. A. Towards deep learning with segregated dendrites. *eLife* **6**, e22901 (2017).
62. Zhao, M., Choi, Y.-S., Obrietan, K. & Dudek, S. M. Synaptic Plasticity (and the Lack Thereof) in Hippocampal CA2 Neurons. *J. Neurosci.* **27**, 12025–12032 (2007).
63. Caruana, D. A., Alexander, G. M. & Dudek, S. M. New insights into the regulation of synaptic plasticity from an unexpected place: Hippocampal area CA2. *Learn. Mem.* **19**, 391–400 (2012).
64. Carstens, K. E. & Dudek, S. M. Regulation of synaptic plasticity in hippocampal area CA2. *Curr. Opin. Neurobiol.* **54**, 194–199 (2019).
65. Aggarwal, A. *et al.* Glutamate indicators with improved activation kinetics and localization for imaging synaptic transmission. *Nat. Methods* **20**, 925–934 (2023).
66. Kolb, I. *et al.* iGABA $\text{SnFR}2$: Improved genetically encoded protein sensors of GABA. *eLife* **14**, RP108319 (2025).

67. Sun, F. *et al.* A Genetically Encoded Fluorescent Sensor Enables Rapid and Specific Detection of Dopamine in Flies, Fish, and Mice. *Cell* **174**, 481-496.e19 (2018).
68. Wang, L. *et al.* A high-performance genetically encoded fluorescent indicator for in vivo cAMP imaging. *Nat. Commun.* **13**, 5363 (2022).
69. Longair, M. H., Baker, D. A. & Armstrong, J. D. Simple Neurite Tracer: open source software for reconstruction, visualization and analysis of neuronal processes. *Bioinformatics* **27**, 2453–2454 (2011).
70. Pnevmatikakis, E. A. & Giovannucci, A. NoRMCorre: An online algorithm for piecewise rigid motion correction of calcium imaging data. *J. Neurosci. Methods* **291**, 83–94 (2017).
71. Magee, J. C. & Johnston, D. Characterization of single voltage-gated Na⁺ and Ca²⁺ channels in apical dendrites of rat CA1 pyramidal neurons. *J. Physiol.* **487**, 67–90 (1995).
72. Avery, R. B. & Johnston, D. Multiple Channel Types Contribute to the Low-Voltage-Activated Calcium Current in Hippocampal CA3 Pyramidal Neurons. *J. Neurosci.* **16**, 5567-5582 (1996).
73. Carlin, K. P., Jiang, Z. & Brownstone, R. M. Characterization of calcium currents in functionally mature mouse spinal motoneurons. *Eur. J. Neurosci.* **12**, 1624–1634 (2000).

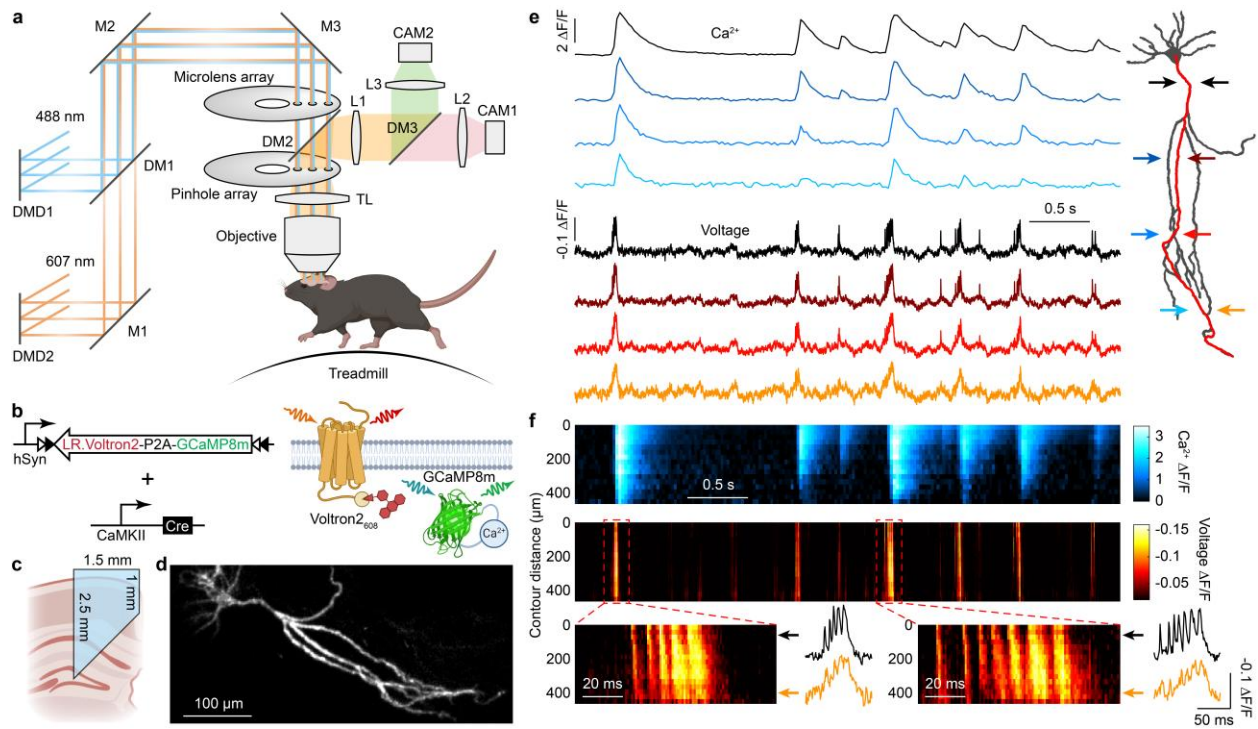


Fig. 1. Simultaneous voltage and Ca^{2+} imaging in dendrites of behaving mice. **a**, A high-speed dual-wavelength imaging system combines micromirror-based patterned illumination with spinning disk confocal microscopy. DMD: digital mirror device; M: mirror; DM: dichroic mirror; L: lens; TL: tube lens; CAM: camera. Relay lenses omitted for simplicity; full diagram in **Fig. S1**. **b**, Genetic construct for sparse co-expression of the voltage indicator Voltron2 and Ca^{2+} indicator jGCaMP8m. **c**, An implanted microp prism provided optical access to the hippocampus. **d**, Single-plane Voltron2-JF608 image of a hippocampal pyramidal neuron acquired *in vivo*. **e**, Simultaneously recorded Ca^{2+} (top) and voltage (bottom) dynamics from soma to distal dendrite (path highlighted on the right) *in vivo*. **f**, Kymographs of Ca^{2+} (top) and voltage (middle) dynamics along the same dendritic branch in **e**. The bottom row shows zoomed-in voltage kymographs and traces for two representative complex spike events.

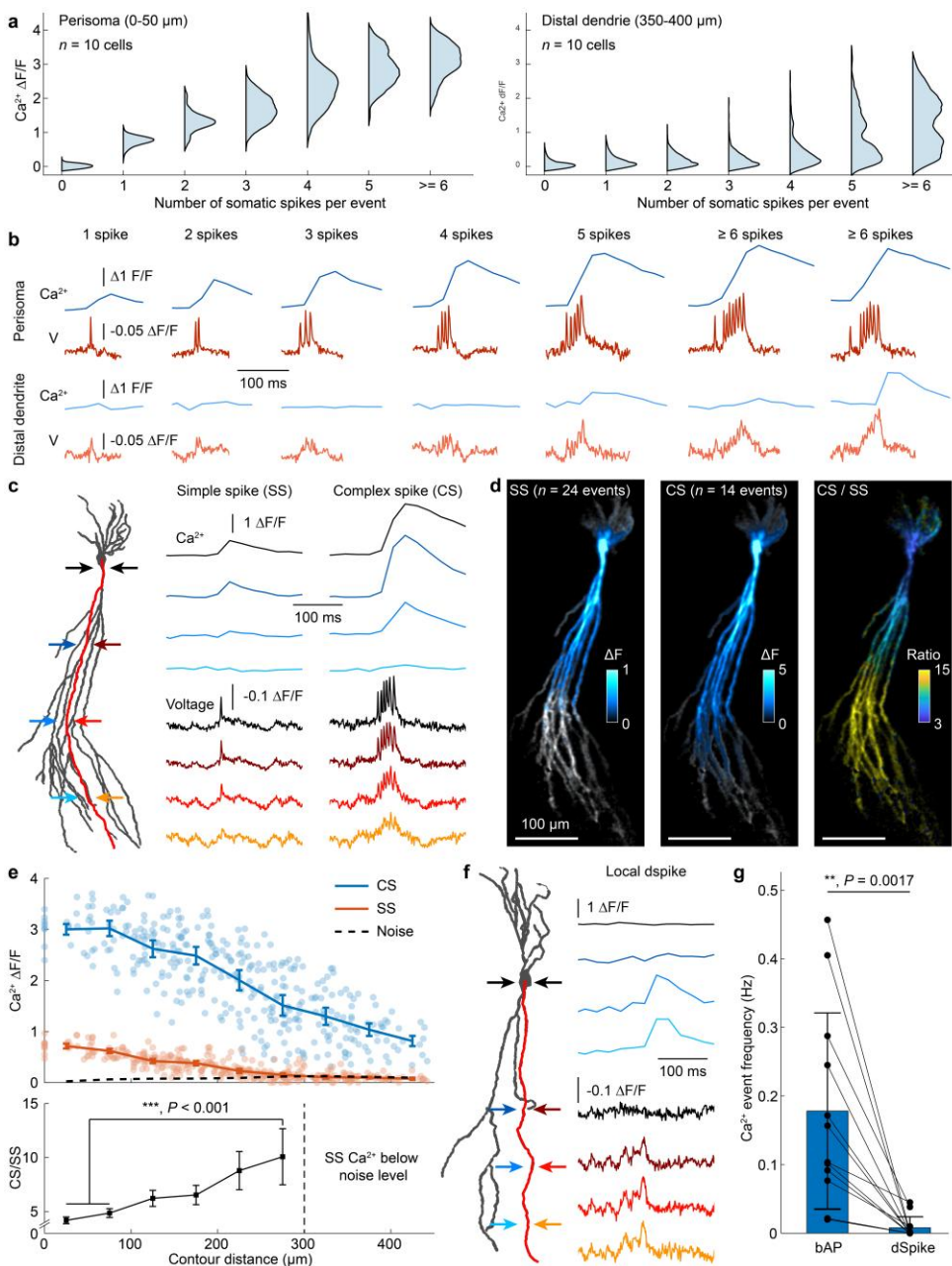


Fig. 2. Distal dendritic Ca^{2+} events primarily come from complex spikes. **a**, Distribution of near-soma (left) and distal dendrite (right) $\text{Ca}^{2+} \Delta F/F$ triggered by events with different numbers of spikes ($n = 10$ cells, 7 mice, 90 – 520 events per category). Neighboring spikes with ≤ 25 -ms intervals were considered the same event. **b**, Representative near-soma (top) and distal dendrite (bottom) Ca^{2+} (blue) and voltage (red) dynamics for events with different numbers of spikes. Events with ≥ 6 spikes sometimes evoked distal Ca^{2+} and sometimes did not. **c**, Representative Ca^{2+} and voltage dynamics during SS (left) and CS (right) back-propagation. **d**, Average Ca^{2+} spatial profiles for SS (left) and CS (middle) events, overlaid on the top of a structural image of the neuron. The right panel shows the ratio between CS and SS. **e**, Top: $\text{Ca}^{2+} \Delta F/F$ for CS and SS events as a function of contour distance from the soma. The noise level was determined by $3 \times \text{s.d.}$ of the silent period (i.e. no Ca^{2+} spikes). Each point represents the average value across all events of the indicated type in a subcellular compartment ($n = 10$ cells, 7 mice). Bottom: Ratio between CS and SS. **f**, Local spike. **g**, Ca^{2+} event frequency (Hz) for bAP and dSpike.

mean CS and SS-induced Ca^{2+} influx as a function of distance from the soma. Data are presented as mean \pm s.e.m. One-way analysis of variance (ANOVA). ***, $P < 0.001$. **f**, Representative Ca^{2+} and voltage dynamics during a local dSpike. **g**, Frequency of bAP-induced Ca^{2+} events and local Ca^{2+} dSpikes. Data are presented as mean \pm s.d. and each point represents one cell ($n = 12$ cells, 9 mice). Paired t-test. **, $P = 0.0017$.

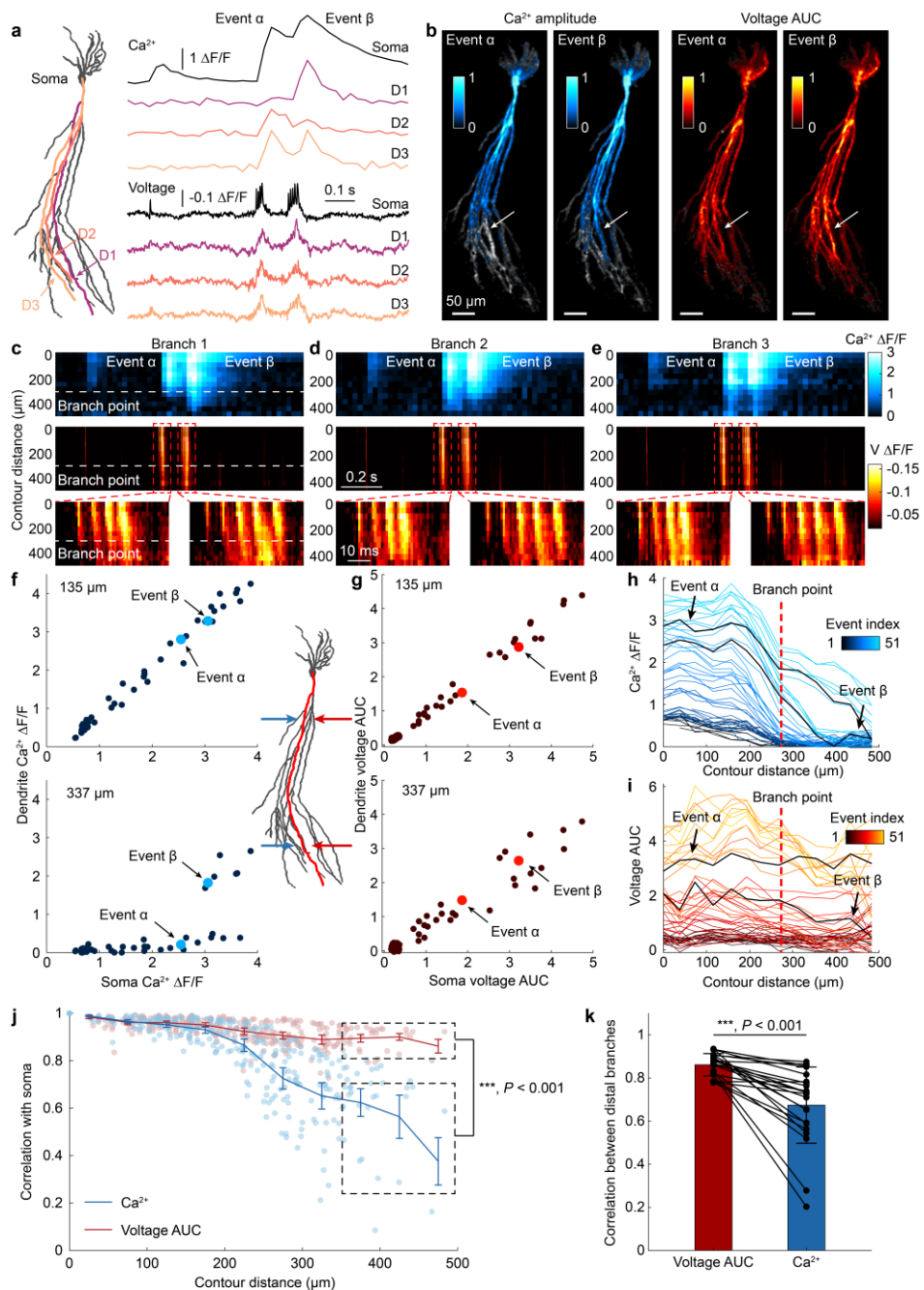


Fig. 3. Small differences in voltage back-propagation lead to large changes in dendritic Ca^{2+} .

a, Representative Ca^{2+} (top) and voltage (bottom) dynamics in the soma and three distal dendrites (highlighted on the left). Events α and β exhibit branch-specific Ca^{2+} signals. **b**, Maps of $\text{Ca}^{2+} \Delta F/F$ (left) and voltage AUC (right) for events α and β , overlaid on a structural image of the neuron. White arrows indicate D1, which shows distinctive Ca^{2+} signals between events. **c-e**, Kymographs of Ca^{2+} (top) and voltage (middle) for events α and β along the same 3 branches as in **a**. The bottom panels show the zoomed-in voltage kymographs for the two events. **f-g**, Dendritic vs. somatic $\text{Ca}^{2+} \Delta F/F$ (**f**) and voltage AUC (**g**) at different contour distances along D1 (highlighted in red). Each data point represents one event. **h-i**, Spatial profiles of $\text{Ca}^{2+} \Delta F/F$ (**h**) and voltage AUC (**i**) along the same dendritic branch as in **f,g**. Each line represents one event. All events are sorted based on

their Ca^{2+} amplitude in the soma. **j**, Correlation coefficients of dendritic Ca^{2+} with somatic Ca^{2+} , and dendritic voltage AUC with somatic voltage AUC, as a function of contour distance. Data are presented as mean \pm s.e.m. and each point represents one subcellular compartment ($n = 10$ cells, 7 mice). Paired t-test. ***, $P < 0.001$. **k**, Correlation coefficients of CS Ca^{2+} and voltage AUC between pairs of distal branches within each cell. Data are presented as mean \pm s.d. and each point represents one pair of distal branches within the same cell (11 – 120 CS events for each pair of distal branches, 22 pairs of distal branches, 10 cells). Paired t-test. ***, $P < 0.001$.

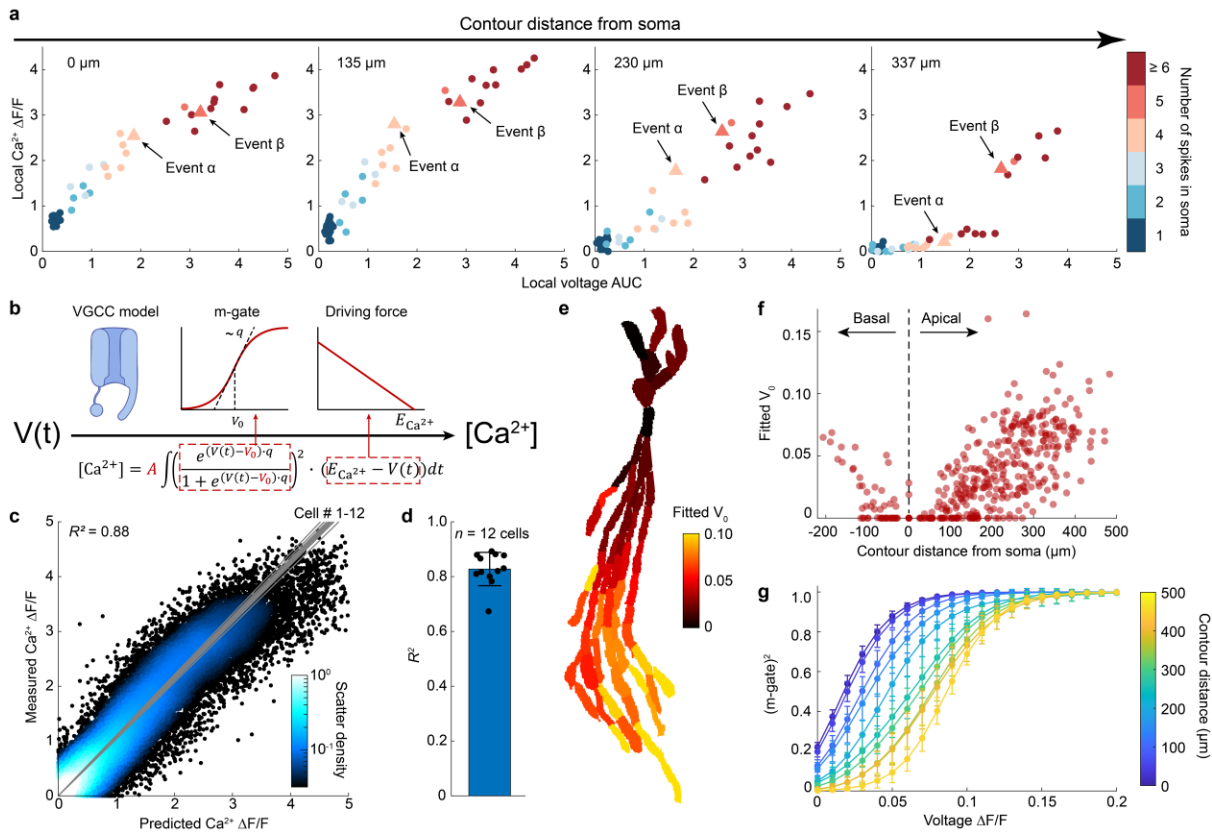


Fig. 4. A simple biophysics-inspired model predicts dendritic Ca^{2+} from local voltage *in vivo*.

a, $\text{Ca}^{2+} \Delta F/F$ vs. local voltage AUC at 4 different subcellular compartments along a single dendritic branch as in **Fig. 3f,g**. Each point represents one event, and the color corresponds to the number of voltage spikes in soma. **b**, Scheme showing the biophysics-inspired model that predicts $\text{Ca}^{2+} \Delta F/F$ from voltage. **c**, Measured $\text{Ca}^{2+} \Delta F/F$ vs. model-predicted $\text{Ca}^{2+} \Delta F/F$ from local voltage waveform. Each point represents one event in a single subcellular compartment ($n = 12$ cells, 476 compartments, 1225 spiking events). Gray lines: linear fit for each cell. **d**, Statistics of the R^2 values for all cells in **c**. Data are presented as mean \pm s.d. and each point represents one cell. **e**, Representative spatial structure of fitted V_0 values across a cell. **f**, Scatterplot of fitted V_0 values as a function of contour distance from soma. Each point represents one subcellular compartment ($n = 10$ cells). **g**, Fitted $(\text{m-gate})^2$ of VGCC as a function of voltage $\Delta F/F$ at different contour distances. Data are presented as mean \pm s.e.m.